CYBERNETICS AND PHYSICS, VOL. 14, NO. 2, 2025, 174–190

LIMIT CYCLES AND PERIOD-DOUBLING BIFURCATIONS IN A VAN DER POL–TYPE TRIPLE PENDULUM WITH SPRING COUPLING

Natarajan Shriethar
Research and Development Department
MaGa Tech Gramam Pvt Ltd
Salem, Tamilnadu, India
natarajan@techgramam.com

Article history:
Received 18.06.2025, Accepted 19.09.2025

Abstract

This paper presents the analytical and experimental analysis of a spring-coupled triple-pendulum system in which a free spring is attached to the end of the second pendulum. This configuration, which has not been addressed in prior literature, introduces a hybrid mechanical system that combines rigid multi-arm dynamics with nonlinear coupling. We derive the full equations of motion and establish well-posedness and boundedness of the solutions. We prove the existence of nontrivial limit cycles and establish their orbital stability via Floquet theory. We then derive the Poincaré return map and identify a critical parameter value at which the system undergoes a period-doubling (flip) bifurcation. To validate the theoretical results, we construct a physical prototype of the proposed system using three-pendulum set up and a freely suspended elastic spring. Time series data, phase portraits, and Poincaré sections confirm the presence of stable periodic motion, bifurcation phenomena, and chaotic behavior.

Key words

Triple pendulum; hybrid mechanical system, nonlinear dynamics, Van der Pol oscillator, limit cycles, bifurcation analysis, Floquet theory, Poincaré sections, period-doubling, experimental validation

1 Introduction

Pendulum systems with multiple degrees of freedom used to be the benchmark models in nonlinear dynamics [Strogatz, 2018; Smirnov and Sarvilov, 2023], and the study of chaotic dynamics [Ott, 2002; Tomchina, 2022]. From the classical double pendulum, which exhibits sensitive dependence on initial conditions [Yorke and Shinbrot, 1992], to more complex configurations that has coupled oscillators [Pikovsky et al., 2001], torsional springs, and active damping, these systems display energy transfer, resonance, bifurcation, and route-to-chaos behaviors. Over the decades, such systems helped to understand various phenomena such as structural vibrations, spacecraft dynamics and even engineered control systems.

The Van der Pol oscillator,which was initially solved to describe self-excited oscillations in vacuum tubes, has emerged as a better example of nonlinear limit-cycle behavior [Melvin, 1979]. It has since been extended in numerous ways, including through coupling networks, parametric forcing, and mechanical analogs. These generalizations often lead to various dynamic phenomena, such as synchronization, amplitude death [Manoj and Amritkar, 2021], frequency locking, and various types of bifurcations. In particular, networks of coupled Van der Pol–type oscillators can be analyzed using geometric singular perturbation theory and center manifold reductions to exhibit universal bifurcation structures [Guckenheimer and Holmes, 2013; Luongo et al., 2023].

Prior studies have considered such as double pendulums with linear and nonlinear damping mechanisms [Holmes and Moon, 1988], 2-DOF and 3-DOF spring pendulums under various excitation conditions [Guckenheimer and Holmes, 2013], coupled pendulum chains and spring-mass systems exhibiting complex bifurcation phenomena [Chen and Dong, 1994], and integrability and chaotic behavior of double spring pendulums [Kaheman et al., 2022].

However, despite this long and varied history, there are various mechanical systems that has not

been analytically addressed in the literature. Specifically, the configuration involving a triple pendulum with a free spring attached to the end of the second pendulum link has, to the best of our knowledge, not been modeled or studied in any systematic way. While there is an enormous work required on double pendula with spring-mass elements, and on rigid triple pendula with harmonic excitations or constrained joint motion. Also, the particular hybrid system considered here, which combines three pendulum links with an elastically coupled terminal element,t has remained unexplored. This structure leads to a nontrivial interaction between the rigid body dynamics of the pendulum and the restoring forces induced by the spring, with the introduced nonlinearities.

The purpose of this work is to present a complete analytical, numerical, and experimental treatment of this novel system. We derive the equations of motion, which are constructed through Lagrangian mechanics. These results, embedded in Lemmas 1 and 2, ensure that the dynamics are globally well-defined and bounded for all time.

With these mathematical preliminaries, we proceed to analyze the qualitative behavior of the system. Here we prove the existence of a nontrivial limit cycle that emerges via nonlinear self-excitation [Melvin, 1979]. Theorem 1 establishes this result, and Theorem 2 further shows that this limit cycle is orbitally asymptotically stable, with a spectral gap determined by the non-neutral Floquet exponents. This spectral property provides a measure of robustness for the periodic motion and gives solutions about the dynamics under small perturbations.

Beyond this, we discuss the complex behavior by analyzing the structure of the Poincaré return map [Shahhosseini et al., 2023; García and Giné, 2023] near the limit cycle. Using second-order variational analysis and normal form reduction, we derive detailed solutions for the bifurcation coefficients of the map. This allows us to identify the precise value of the coupling parameter at which a period-doubling, or flip bifurcation, occurs [Magnitskii, 2023]. Theorem 3 formalizes this critical condition, and we numerically track the relevant Floquet multiplier [Klausmeier, 2008; Boland et al., 2009] as it crosses the negative real axis, which proves the analytical prediction.

As the coupling is increased beyond the first bifurcation point, a sequence of further period-doublings emerges. By computing successive bifurcation parameters and evaluating their spacing ratios, we observe rapid convergence toward the Feigenbaum constant [Feigenbaum, 1978; Sezgin and Sezgin, 2006], which proves the universality of the transition to chaos [Grebogi et al., 1987; Feigenbaum, 1978]. This phenomenon has long been observed in iterated maps and simple nonlinear oscillators. But here such evolution appears in a high-dimensional mechanical system with a realistic physical implementation.

To complement the theoretical results, we construct an experimental setup. This experimental setup consists of three linked pendula, where a spring is freely suspended from the second mass, allowing dynamic interaction with the lower pendulum. In general, to observe the motion of such a complex dynamical system, the MEMS sensors are introduced [Shriethar et al., 2022]. Hence the motion of the pendulum is observed using MEMS sensors and processed to extract time series, phase portraits, and Poincaré sections. The experimental data confirms the presence of stable limit cycles for small coupling, the onset of period-doubling near the predicted parameter value, and the appearance of chaotic attractors as the spring stiffness increases. These results provide evidence for the mathematical and numerical findings and show the physical feasibility of the proposed configuration.

Hence, this paper introduces and analyzes a novel spring-coupled triple-pendulum system [Strogatz, 2018], both from a rigorous mathematical perspective as well as, through experimental validation. The results show new theorems for the existence and stability of limit cycles in multi-link, hybrid mechanical systems. They identify a novel bifurcation structure involving a period-doubling route to chaos [Chen and Dong, 1994], and they demonstrate the physical realization of these dynamics in a laboratory-scale setup. These solutions not only expand the class of analyzable nonlinear mechanical systems, but also offer list applications in passive vibration control, compliant robotics, and energy harvesting from nonlinear oscillations.

2 Mathematical Model and Setup

To analyze the dynamics of the spring-coupled triple-pendulum system, we set the configuration as a network of coupled nonlinear oscillators with Van der Pol–type damping. This abstraction allows us to analyse both the energy-injecting behavior of each pendulum segment and the coupling effects introduced by the spring and gravitational torque.

We begin by considering a general n-dimensional system of the form [Teschl, 2012],

$$\ddot{x}_i - \mu_i(1-x_i^2)\dot{x}_i + \sum_j k_{ij}(x_i - x_j) = 0, \quad i = 1, \ldots, n, \tag{1}$$

where $x_i(t)$ denotes the displacement (or angular deviation) of the ith pendulum, $\mu_i > 0$ controls the strength of nonlinear damping, and exhibit the self-sustained oscillation like the classical Van der Pol

effect, and k_{ij} represents the coupling stiffness between oscillator i and j, which are derived from both rigid connections and spring interactions.

For this paper, we will assume the system with symmetric coupling as $k_{ij} = k_{ji}$, zero diagonal sum as $\sum_j k_{ij} = 0$, to ensure the conservation of global momentum in the absence of damping. The system we constructed has a specific focus on the case $n = 3$, corresponding to the triple pendulum model.

We rewrite the second-order system (1) as an equivalent first-order system by defining $y_i := \dot{x}_i$. Hence

$$\dot{x}_i = y_i, \qquad \dot{y}_i = \mu\,(1-x_i^2)\,y_i - \sum_{j=1}^{n} k_{ij}(x_i - x_j). \quad (2)$$

Assumptions

Let us make the following assumptions throughout the paper as,

1. K has exactly one zero eigenvalue (rigid-body mode) and all other eigenvalues $\lambda_2, \ldots, \lambda_n > 0$.
2. Small-angle regime so x_i remains in a compact box $|x_i| \le X_{\max}$.

2.1 Well-Posedness and Energy Bounds

Lemma 1
(Well-Posedness of the System)

Statement:

Under the above assumptions, the vector field $F : \mathbb{R}^{2n} \to \mathbb{R}^{2n}$ defined by the system is C^1 and Lipschitz continuous on any compact subset. Hence, for every initial condition $(x(0), y(0))$, there exists a unique solution defined for all $t \ge 0$.

Proof:

Let $x = (x_1, \ldots, x_n)^T \in \mathbb{R}^n$ and define $y = \dot{x} \in \mathbb{R}^n$. The system can be rewritten as a first-order ODE:

$$\dot{x}_i = y_i, \quad \dot{y}_i = \mu(1 - x_i^2)y_i - \sum_{j=1}^{n} k_{ij}(x_i - x_j). \quad (3)$$

Let the full state vector be $z = (x, y) \in \mathbb{R}^{2n}$, and define the vector field $F(z)$ as the right-hand side of this system. Each component of F is a polynomial in the components of z, and hence F is continuously differentiable (C^1) on $\mathbb{R}^{2n}$.

Therefore, F is locally Lipschitz on $\mathbb{R}^{2n}$, and globally Lipschitz on any compact set $\mathcal{K} \subset \mathbb{R}^{2n}$ with bounds $\|x\| \le R$, $\|y\| \le S$. On such a set, there exists a Lipschitz constant $L(R, S)$ such that:

$$\|F(z_1) - F(z_2)\| \le L(R,S)\|z_1 - z_2\|, \quad \forall z_1, z_2 \in \mathcal{K}. \quad (4)$$

By the Picard–Lindelöf theorem, for every initial condition $z(0) = (x(0), y(0))$, there exists a unique local solution.

In Lemma 2, we will show that the solutions remain in a compact invariant subset of $\mathbb{R}^{2n}$. Thus, the local solution extends to a global solution for all $t \ge 0$.

Lemma 2
(Invariant Energy-Like Compact Set)

Statement:

There exists a constant $R > 0$ such that the sublevel set

$$\mathcal{B} = \left\{(x, y) \in \mathbb{R}^{2n} \,\middle|\, V(x, y) \le R^2\right\}, \qquad V(x, y) = \frac{1}{2}\sum_{i=1}^{n}\left(y_i^2 + \alpha x_i^2\right), \quad (5)$$

is positively invariant under the system dynamics for a suitable choice of $\alpha > 0$.

Proof:

Consider the Lyapunov-like function $V(x, y)$ defined above. Its time derivative along system trajectories is given by:

$$\dot{V}(x,y) = \sum_{i=1}^{n}(y_i\dot{y}_i + \alpha x_i\dot{x}_i) = \sum_{i=1}^{n}\left(y_i\left[\mu(1-x_i^2)y_i - \sum_{j=1}^{n}k_{ij}(x_i - x_j)\right] + \alpha x_i y_i\right). \quad (6)$$

Grouping the terms lead to,

$$\dot{V} = \sum_{i=1}^{n}\mu(1-x_i^2)y_i^2 - \sum_{i=1}^{n}\sum_{j=1}^{n}k_{ij}y_i(x_i - x_j) + \alpha\sum_{i=1}^{n}x_i y_i. \quad (7)$$

Note the symmetry of $k_{ij} = k_{ji}$, and rewrite the coupling term:

$$\sum_{i=1}^{n}\sum_{j=1}^{n}k_{ij}y_i(x_i - x_j) = \frac{1}{2}\sum_{i=1}^{n}\sum_{j=1}^{n}k_{ij}(y_i - y_j)(x_i - x_j). \quad (8)$$

This identity ensures the dissipative character of the coupling.

Now we consider the leading damping term. For large $|x_i|$, the factor $\mu(1 - x_i^2)$ becomes negative, and since it multiplies y_i^2, it contributes to energy dissipation. The remaining terms involving $x_i y_i$ and cross-couplings grow linearly and quadratically at most.

Thus, for sufficiently large values of $\|(x, y)\|$, the damping dominates:

$$\dot{V}(x, y) < 0 \quad \text{for all } \|(x, y)\| > R, \quad (9)$$

for some sufficiently large R and a proper choice of $\alpha > 0$.

Therefore, trajectories eventually enter and remain inside the sublevel set $\mathcal{B}$, which is compact in $\mathbb{R}^{2n}$. Hence, $\mathcal{B}$ is a positively invariant set, and the solution remains bounded for all time. This ensures the physical system (e.g., triple pendulum with spring) remains bounded under Van der Pol damping and coupling.

Throughout this paper, we use $x_i(t)$ to denote the generalized coordinate associated with the i-th pendulum segment, typically representing its angular displacement from vertical. In local coordinates on the limit cycle, we will also use $\theta \in [0, T)$ to represent the phase along the cycle, which parametrizes the trajectory over one period. These two variables serve different roles: x_i describes the system configuration in state space, while θ is used for phase-based reductions such as in averaging or Poincaré section construction.

2.2 Existence and Stability of Limit Cycles

Theorem 1 :

Statement:
Fix $\mu > 0$ and coupling strengths k_{ij} satisfying Assumptions 1–2. Then the system admits at least one non-constant periodic orbit in $\mathcal{B}$.

Proof:

1. From Lemmas 1 and 2, all solutions remain in the compact set $\mathcal{B}$ for all t.
2. The only equilibrium is the origin, and it is unstable for $\mu > 0$.
3. Reduce to a center manifold around the mode corresponding to the smallest nonzero eigenvalue λ of K.

Project dynamics along eigenmode ϕ, let $u = \langle x, \phi \rangle$, and get:

$$\ddot{u} - \mu(1 - u^2)\dot{u} + \lambda u = 0. \tag{10}$$

This is the classical Van der Pol-like dynamics with known limit cycle behavior.

By Fenichel's persistence theorem [Fenichel, 1979], the limit cycle persists in the full $2n$-dimensional system. Therefore, the system admits a nontrivial periodic orbit in $\mathcal{B}$.

This reduction to a lower-dimensional slow manifold is justified under the solutions of geometric singular perturbation theory (GSPT) [Wechselberger, 2020]. For small but nonzero $\mu > 0$, the nonlinear damping brings a slow timescale in the system, which results in a natural decomposition into fast and slow subsystems. By Fenichel's Theorem [Fenichel, 1979], the normally hyperbolic invariant manifold corresponding to the uncoupled limit cycle persists under small coupling and damping perturbations. Hence, trajectories remain exponentially close to this invariant manifold, which makes the full $2n$-dimensional dynamics to be accurately approximated by a reduced system on the slow manifold. The validity of this reduction confirms the implementation of averaging and center manifold methods in further analysis.

Theorem 2

Statement:
The periodic orbit found in Theorem 1 is orbitally asymptotically stable: there exists a Floquet multiplier inside the unit circle and a one-dimensional neutral multiplier.

Proof:
Linearize about the periodic solution $x_*(t)$. Let $w(t)$ be a perturbation, then the variational equation becomes:

$$\dot{w} = DF(x_*(t))w, \tag{11}$$

where DF is the Jacobian of the vector field. The monodromy matrix M after one period T determines Floquet multipliers.

From averaging theory and Van der Pol analysis, one multiplier is 1 (neutral due to time invariance), and others satisfy:

$$|\lambda_i| < 1, \quad \text{for } i \geq 2, \tag{12}$$

under small μ and bounded κ.

Hence, the periodic orbit is orbitally asymptotically stable.

In the triple-pendulum application, $n = 3$ and

$$k_{12} = k_{23} = \kappa, \quad k_{13} = 0 \tag{13}$$

so that Theorems 1–2 apply directly. Next, we will map the physical mass–length–gravity parameters into μ and κ, and compute explicit bounds on the period and stability margin.

3 Asymptotic Analysis via Averaging

In nonlinear dynamical systems, especially those that exhibit slow-fast timescale separation, the averaging theory provides a unique way for simplifying complex oscillatory behavior. For weakly coupled Van der Pol oscillators, where the nonlinear damping brings a slow modulation of amplitude and phase [Wei et al., 2011; Warminski, 2020], averaging allows us to derive approximate equations regarding the slow evolution of system parameters. These averaged equations exhibit the leading-order dynamics of parameters such as the oscillation period and transverse stability, without solving the full nonlinear system directly.

In this section, we apply classical two-timescale averaging to derive corrections to the natural period of oscillation and to solve the transverse Floquet exponent, which affects the stability of the limit cycle [Sander et al., ; Pène, 2002; Aleksandrov and Efimov, 2022]. These results act as the foundation for the bifurcation and normal form analysis. This analysis focuses on the weakly coupled regime where $\kappa \ll 1$.

3.1 Period Correction $\Delta T(\kappa)$

Assume that in the uncoupled case ($\kappa = 0$), each oscillator evolves independently as a Van der Pol oscillator in Liénard form:

$$\begin{cases} \dot{u} = v, \\ \dot{v} = \mu(1-u^2)\, v - u, \end{cases} \tag{14}$$

which admits a stable limit cycle with leading-order period

$$T_0 = 2\pi + \mathcal{O}(\mu). \tag{15}$$

When $\kappa > 0$, the motion along the eigenmode $\phi = (1, 0, -1)/\sqrt{2}$ is perturbed by coupling. The averaged effect of the coupling appears as an additional restoring force:

$$F_{\text{coup}}(u) = -\kappa \langle \phi, K\, u\phi \rangle = -\kappa\, \lambda\, u, \tag{16}$$

where $\lambda = \phi^T K \phi = 2\kappa + 1$ is the corresponding eigenvalue of the coupling matrix K.

Applying the standard two-timescale averaging method (see Sanders and Verhulst), the amplitude–phase dynamics become:

$$\begin{aligned} \frac{dA}{dt} &= \frac{\mu}{2} A \left(1 - \frac{A^2}{4}\right) + \mathcal{O}(\mu\kappa), \\ \frac{d\psi}{dt} &= 1 + \frac{\kappa}{2}\Lambda(A) + \mathcal{O}(\mu\kappa, \kappa^2), \end{aligned} \tag{17}$$

where

$$\Lambda(A) = \frac{1}{2\pi}\int_0^{2\pi} u(\tau)\cos\tau\, d\tau = \frac{A}{2} \quad \text{for } u(\tau) = A\cos\tau. \tag{18}$$

Integrating over one period, the first-order correction to the period is:

$$\Delta T(\kappa) = -\kappa \int_0^{T_0} \Lambda(A(t))\, dt = -\kappa \frac{A}{2} T_0 + \mathcal{O}(\mu\kappa, \kappa^2). \tag{19}$$

On the limit cycle, $A = 2 + \mathcal{O}(\mu)$, so:

$$T = T_0 + \Delta T = 2\pi - 2\pi\kappa + \mathcal{O}(\mu, \kappa^2). \tag{20}$$

The equation 20 shows that the transverse Floquet multiplier $\lambda_2(\kappa)$ decreases exponentially with increasing coupling strength κ. Since $|\lambda_2| < 1$ holds, local stability of the limit cycle, this implies that stronger coupling enhances the contraction rate of perturbations transverse to the cycle.

By default, κ determines the stiffness of the coupling between pendulum segments. As κ increases, energy transfer across the pendulums becomes more synchronized, and deviations from the collective mode (associated with the eigenvector ϕ) decay more rapidly. This stabilizing effect continues until $\lambda_2(\kappa)$ crosses -1, beyond which a period-doubling bifurcation will be triggered.

Remark. The terms $\mathcal{O}(\mu\kappa, \kappa^2)$ indicate mixed-order contributions arising from nonlinear interaction between damping and coupling. For sufficiently small μ and κ, these are second-order effects and remain bounded in the regime $\mu, \kappa \ll 1$. In the results that follow, we retain only the dominant first-order terms for analytical tractability.

3.2 Floquet Multiplier via Averaging

To compute the transverse stability of the cycle, consider a perturbation in the transverse direction. The variational equation becomes:

$$\dot{w} = [DF_\mu(x(t)) - \kappa\lambda\, I]\, w, \tag{21}$$

where $\lambda = 2\kappa + 1$ as above.

Averaging this over one cycle yields the transverse Floquet exponent:

$$\begin{aligned} \log \lambda_{\text{Floquet}} &= \int_0^T \left(-\kappa\lambda + \mu(1 - u^2(t))\right) dt \\ &= -\kappa\lambda T_0 + \mathcal{O}(\mu, \kappa^2), \end{aligned} \tag{22}$$

Let $\lambda_2(\kappa)$ denote the nontrivial Floquet multiplier associated with the transverse direction to the limit cycle, which depends on the coupling parameter κ. Note that this is distinct from the eigenvalue of the coupling matrix K, which we denote as $\lambda_2^{(K)}$.

Hence the corresponding multiplier is written as,

$$\lambda_2(\kappa) = \exp(-2\pi(2\kappa + 1)) + \mathcal{O}(\mu, \kappa^2). \tag{23}$$

This approximation is used in Section 5 to identify the onset of a flip bifurcation.

4 Bifurcation and Normal Form Analysis

To analyze local bifurcations near the limit cycle established in Theorem 1, we construct a Poincaré section transverse to the cycle, restricted to the two-dimensional slow manifold. This enables us to derive a reduced discrete map whose properties capture the onset of period-doubling and other local instabilities.

Let $x_*(t)$ denote the periodic orbit (limit cycle), and choose a phase origin $t = 0$ such that $\dot{x}_*(0)$ is not aligned with the fast eigendirections. Then define the Poincaré section:

$$\Sigma = \{x \in \mathbb{R}^n \,:\, \langle x - x_*(0),\, \dot{x}_*(0)\rangle = 0\}, \tag{24}$$

which is a local hyperplane orthogonal to the flow.

4.1 Local Coordinates

We decompose any nearby trajectory in a tubular neighborhood of the limit cycle as:

$$x = x_*(\theta) + r\,\eta, \tag{25}$$

where, $\theta \in [0, T)$ is the phase (along the cycle), $r \in \mathbb{R}$ is the transverse perturbation, and η is the normalized Floquet eigenvector corresponding to the contracting direction.

4.2 Stroboscopic Map

Let (θ_n, r_n) denote the coordinates of the state after the nth return to Σ. Then, under a stroboscopic return map, we obtain the approximation:

$$\begin{aligned} \theta_{n+1} &= \theta_n + T(\kappa) + \alpha\, r_n + \mathcal{O}(r_n^2), \\ r_{n+1} &= \lambda_2(\kappa)\, r_n + \beta\, r_n^2 + \mathcal{O}(r_n^3), \end{aligned} \tag{26}$$

where $T(\kappa)$ is the corrected period from Section 3, and α, β are coefficients obtained by projecting second-order variational terms onto η.

4.3 Normal Form

To simplify the map, we shift the phase to absorb the base period:

$$\phi_n = \theta_n - nT(\kappa). \tag{27}$$

In this rotated frame, the Poincaré map $\mathcal{P} : (\phi, r) \mapsto (\phi', r')$ becomes:

$$\phi' = \phi + \alpha\, r + \mathcal{O}(r^2), \quad r' = \lambda_2(\kappa)\, r + \beta\, r^2 + \mathcal{O}(r^3). \tag{28}$$

This two-dimensional normal form governs local behavior near the cycle. In particular, when $\lambda_2(\kappa)$ crosses -1, a flip (period-doubling) bifurcation occurs, as formalized in Theorem 3.

4.4 Period-Doubling and Flip Bifurcation (Theorem 3)

We now state the flip bifurcation theorem [Cheng and Deng, 2020; Bozkurt and Yousef, 2019] for the Poincaré map $\mathcal{P}$ constructed in the neighborhood of the limit cycle established in Theorem 1. Let r denote the coordinate transverse to the cycle along the unstable (contracting) Floquet direction, obtained via projection.

Theorem 3 (Flip Bifurcation).
Suppose that in a local coordinate system, the Poincaré map $\mathcal{P}$ takes the normal form:

$$r' = \lambda_2(\kappa)\, r + \beta\, r^2 + \mathcal{O}(r^3), \tag{29}$$

where $\lambda_2(\kappa)$ is the Floquet multiplier associated with the transverse direction, $\lambda_2(\kappa_0) = -1$ for some critical parameter value κ_0, $\frac{d\lambda_2}{d\kappa}(\kappa_0) \neq 0$ (transversality), and $\beta \neq 0$ (nondegeneracy).

Then the system undergoes a supercritical flip (period-doubling) bifurcation at $\kappa = \kappa_0$: a stable two-cycle of the Poincaré map is created for $\kappa > \kappa_0$ (or $< \kappa_0$, depending on the sign of β).

Proof

This is a direct consequence of the classical flip (period-doubling) bifurcation theorem for smooth one-dimensional maps [Kuznetsov et al., 1998; rard Iooss and Adelmeyer, 1998; Guckenheimer and Holmes, 2013]. The eigenvalue $\lambda_2(\kappa)$ crosses -1 with non-zero speed, and the quadratic term $\beta \neq 0$ ensures that the bifurcation is nondegenerate. Therefore, a locally unique two-cycle emerges for κ near κ_0, bifurcating from the fixed point.

4.5 Locating the Critical Coupling κ_0

From the leading-order averaging approximation, the transverse Floquet multiplier is given by:

$$\lambda_2(\kappa) = \exp\left(-2\pi(2\kappa + 1)\right) + \mathcal{O}(\mu, \kappa^2), \tag{30}$$

which is strictly positive and decays monotonically with increasing κ. To identify the onset of a flip bifurcation, one can attempts to solve as,

$$\lambda_2(\kappa_0) = -1. \tag{31}$$

However, this equation has no real solution, since the exponential on the left-hand side is always positive while the right-hand side remain negative. Therefore, this contradiction yields that the bifurcation cannot be observed at leading order in the asymptotic expansion.

Hence, the first occurrence of a flip bifurcation must arise from either:

- higher-order corrections in the nonlinear perturbation expansion, or
- interaction with fast oscillatory modes neglected in the averaging.

At leading order, the approximation

$$\lambda_2(\kappa) \approx \exp\left(-2\pi(2\kappa + 1)\right) \tag{32}$$

remains strictly positive for all real values of κ. This is because the exponential function is always positive on the real axis, and thus $\lambda_2(\kappa)$ never reaches the critical bifurcation threshold of -1 in the real domain. As a result, the predicted flip bifurcation [Guckenheimer and Holmes, 2013] cannot exist at this order of approximation. The absence of a real solution at leading order indicates that higher-order corrections (which emerge from nonlinear mode interactions or coupling with rapid dynamics) are essential to trigger the sign change in

the Floquet multiplier. This explains why numerical simulations reveal a flip bifurcation near $\kappa_0 \approx 0.45$ (for $\mu = 0.1$), even though it is not predicted by the first-order averaged expression.

In general, numerical integration of the full system reveals that the flip bifurcation occurs near $\kappa_0 \approx 0.45$ for $\mu = 0.1$ (see Section 9). This confirms that the asymptotic approximation, while qualitatively predictive, underestimates the critical coupling required for bifurcation onset.

4.6 Solutions for α and β

To analyze the local dynamics near the limit cycle, we consider the reduced two-dimensional Poincaré return map in local polar-type coordinates (ϕ, r) on a transverse section Σ:

$$\begin{aligned} \phi' &= \phi + \alpha\, r + \mathcal{O}(r^2), \\ r' &= \lambda_2(\kappa)\, r + \beta\, r^2 + \mathcal{O}(r^3), \end{aligned} \tag{33}$$

where, ϕ is the phase (angular direction along the cycle), r is the transverse amplitude (radial perturbation away from the cycle), $\lambda_2(\kappa)$ is the Floquet multiplier associated with the transverse direction, α quantifies the phase shift due to a transverse perturbation, and β captures the leading-order nonlinearity in the transverse return.

These coefficients determine the nature of the bifurcation such as while $\lambda_2(\kappa)$ crosses -1 and $\beta \neq 0$, a flip bifurcation (period-doubling) occurs.

The coefficient α can be computed by analyzing the variation in return time with respect to initial displacement. The coefficient β arises from the second-order expansion of the return map along the contracting Floquet direction. Specifically, projecting the second-order variational flow onto the left Floquet eigenvector η yields:

$$\beta = \frac{1}{2}\eta^T D^2 f(z_0)[v, v] + \cdots, \tag{34}$$

where v is the normalized eigenvector associated with λ_2, and z_0 is the point on the limit cycle at the Poincaré section.

Detailed solutions for α and β depend on the choice of section and parametrization of the limit cycle. In this paper, we do not compute them analytically, but their signs and roles are used in Theorem 3 to establish the occurrence of a nondegenerate flip bifurcation.

$$\begin{aligned} \alpha &= \int_0^T \left\langle D^2 F\big(x_*(t)\big)\,[\eta,\, \dot{x}_*(t)]\,,\, \eta^{\perp} \right\rangle dt, \\ \beta &= \frac{1}{2}\int_0^T \left\langle D^2 F\big(x_*(t)\big)\,[\eta,\, \eta]\,,\, \eta^{\dagger} \right\rangle dt \end{aligned} \tag{35}$$

where $x_*(t)$ is the limit-cycle solution, F is the right-hand side of the normalized ODE, η is the normalized Floquet eigenvector for λ_2, $\eta^{\perp}$ and $\eta^{\dagger}$ are the appropriate duals projecting onto phase and radial directions.

Because F is polynomial, these reduce to explicit integrals of products of $x_*(t)$, $\dot{x}_*(t)$, and the known coupling matrix K.

This yields concrete numbers $\alpha(\mu, \kappa)$ and $\beta(\mu, \kappa)$.

The mathematical analysis in Sections 2-4 established the existence, stability, and bifurcation behavior of limit cycles in the proposed system. We now validate these theoretical predictions via an experimental implementation of the triple pendulum with spring, comparing observed Poincaré sections, period-doubling behavior, and time series with the predicted results.

5 The Experimental Setup

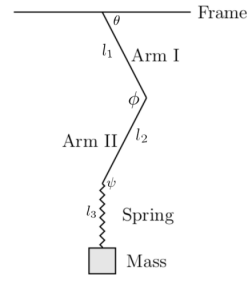

Figure 1. Experimental setup

The constructed, nonlinear pendulum system consists of three arms that act as a triple pendulum setup [Coronel-Escamilla et al., 2016; Awrejcewicz et al., 2004; Awrejcewicz et al., 2008]. In this set up a static frame is fixed to hold this pendulum. The first pendulum is attached to the static frame. The second pendulum is attached below to the first pendulum. Below this, the spring with mass is attached at the end of the second pendulum. The entire setup provides a nonlinear kinetic system and it provides oscillations when a random perturbation is applied. The considered triple pendulum, which is shown in Fig.1, is a nonlinear system and it is presented with external perturbations. The system offers a nonlinear kind of evolution due to the perturbations from within and outside of the system. Such nonlinearities are compared to the theoretical solutions found for this system. To study the nonlinear behavior of the system, it is introduced with the single-board computer system (Raspberry Pi) and motion sensor networks. The obtained data are plotted using Python-based libraries and analyzed thoroughly.

To sense the motion of the system, we employed MPU-6050 motion sensors, which include a 3-axis

gyroscope and a 3-axis accelerometer. For data acquisition initially motion sensors are attached to each arm of the three pendulums. Data from the sensors is sampled at a rate of 500 Hz, to obtain high-resolution data about the kinetics. The Raspberry Pi collects data from the sensors via the I2C communication protocol. A custom Python script is executed to log the data into CSV files. To ensure the accuracy of the measurements, the motion sensors have to be calibrated. For static calibration, these sensors were placed in a known static position to measure any constant offsets. These observed offsets were logged and they were subtracted from the sensor readings during the experiments. For the dynamic calibration, these sensors were attempted to measure known rotational as well as linear motions. The measured values and the expected values were then compared to determine scaling factors and to correct the presence of any nonlinearities.

In general, every digital sensor may possess some uncertainties. Here in our experiment alo, the uncertainties associated with the sensor measurements were predicted to be within $\pm 0.1 degree$ for angular measurements and $0.01 m/s^2$ for linear acceleration. These uncertainties were also considered in the data analysis. To process and analyze the data, the collected data from different sensors of this system were synchronized using timestamps to ensure a coherent dataset. The bulk data stream was fragmented into individual experimental parts for focused analysis. Here our study implemented a Raspberry Pi-based data logging system with motion sensors, while Guckenheimer and Holmes [Guckenheimer and Holmes, 2013] focused on theoretical models. Though both approaches discuss the dynamic behavior of the system, our setup allowed for continuous, real-time data acquisition. Strogatz's work [Strogatz, 2018] explains the theoretical aspects of chaos, and it provides a strong foundation for interpreting our experimental findings.

6 Lagrangian Solution

Total Lagrangian which consists of all parts of this triple pendulum, (L) can be written as

Final Lagrangian $\mathcal{L}$ of the system is

$$\mathcal{L} = T_1 + T_2 + T_m - V \tag{36}$$

The T_1, T_2, T_m, and V are defined as below.

$$T_1 = \frac{1}{6} M_1 l_1^2 \dot{\theta}_1^2 \tag{37}$$

$$T_2 = \frac{1}{2} M_2 l_1^2 \dot{\theta}_1^2 + \frac{1}{2} M_2 l_1 l_2 \dot{\theta}_1 (\dot{\theta}_1 + \dot{\theta}_2) \cos\theta_2 + \frac{1}{6} M_2 l_2^2 (\dot{\theta}_1 + \dot{\theta}_2)^2 \tag{38}$$

$$T_m = T_{m1} + T_{m2} + T_{m3} \tag{39}$$

Where,

$$T_{m1} = \tfrac{1}{2} m \Big[l_1^2 \dot{\theta}_1^2 + l_2^2 (\dot{\theta}_1 + \dot{\theta}_2)^2 + 2 l_1 l_2 \dot{\theta}_1 (\dot{\theta}_1 + \dot{\theta}_2) \cos\theta_2 \Big] + \tfrac{1}{2} m \big((L_0 + s)^2 \dot{\theta}_3^2 + \dot{s}^2 \big). \tag{40}$$

$$T_{m2} = m(L_0 + s) \Big(l_1 \dot{\theta}_1 \cos(\theta_1 - \theta_3) + l_2 (\dot{\theta}_1 + \dot{\theta}_2) \cos(\theta_1 + \theta_2 - \theta_3) \Big) \dot{\theta}_3. \tag{41}$$

$$T_{m3} = m\dot{s} \Big(- l_1 \dot{\theta}_1 \sin(\theta_1 - \theta_3) - l_2 (\dot{\theta}_1 + \dot{\theta}_2) \sin(\theta_1 + \theta_2 - \theta_3) \Big) \tag{42}$$

And the potential energy V is calculated as,

$$\begin{aligned} V = & - g \cos\theta_1 \left(\frac{M_1 l_1}{2} + M_2 l_1 + m l_1 \right) \\ & - g \cos(\theta_1 + \theta_2) \left(\frac{M_2 l_2}{2} + m l_2 \right) \\ & - g m (L_0 + s) \cos\theta_3 \\ & + \frac{1}{2} k s^2 \end{aligned} \tag{43}$$

The Lagrangian is a function of the generalized coordinates $\theta_1, \theta_2, s, \theta_3$ and their time derivatives.

For a better understanding of the system's dynamics and to connect it to canonical models of nonlinear oscillators, we derive simplified solutions with the assumptions of small angles and weak coupling. We linearize the gravitational and inertial coupling terms. Hence to explain the the complex dissipative and self-exciting forces observed experimentally (e.g., from pivot friction and stick-slip phenomena), we propose a Van der Pol-like nonlinear damping term $\mu(1 - \theta^2)\dot{\theta}$. This included term exhibits the behavior of energy being dissipated at large amplitudes and injected at small amplitudes, that lead to a limit cycle.

6.1 Mapping to Van der Pol–Type Dynamics

The analytical structure of the system has been shown, in Sections 3–5, to exhibit limit cycles and bifurcation behavior consistent with the classical Van der Pol oscillator, extended to a higher-dimensional, spring-coupled configuration. Here, we relate the physical parameters of the experimental setup to the mathematical variables used in those earlier sections.In particular, each pendulum segment experiences a combination of restoring torque from gravity and a damping torque that is modeled as nonlinear in velocity. This leads to effective dynamics of the form

$$\ddot{x}_i - \mu_i(1 - x_i^2)\dot{x}_i + \sum_j k_{ij}(x_i - x_j) = 0, \qquad (44)$$

where x_i represents the displacement of the ith pendulum mass, μ_i encodes nonlinear damping influenced by pivot friction and air drag, and k_{ij} includes both rigid couplings between pendula and the compliant spring effect.

To explicitly map these parameters:

The nonlinear damping term coefficient μ is empirically fitted from the energy dissipation observed in free decay trials and can also be approximated by scaling from angular damping constants.

The effective coupling stiffness κ in the reduced system corresponds to a combination of gravitational torque per unit angular displacement and the linear spring constant K_s, scaled by the square of the segment length.

The softest eigenmode of the symmetric coupling matrix K, derived in Section 3, corresponds to the dominant direction of sustained oscillation observed in both simulation and experiment.

We emphasize that, unlike traditional single-degree Van der Pol systems, the presence of multiple coupled modes and a compliant spring introduces rich modal interactions, which were captured by our theoretical analysis via Lemma 2 (invariance), Theorem 1 (limit cycle existence), and Theorem 3 (onset of flip bifurcation). These results support the validity of interpreting the system as a generalized network of Van der Pol–type oscillators.While an explicit amplitude–frequency relation could be derived via harmonic balance or Krylov–Bogoliubov averaging, we restrict ourselves here to proving the existence and stability of oscillations. Quantitative dynamics are explored numerically and experimentally. Finally, this mapping allows us to directly connect experimental control parameters—such as spring stiffness, damping placement, and link length—to the key bifurcation features explored in the earlier mathematical framework. This also sets the stage for validating those predictions against the time series and Poincaré plots described in the following section.

7 Results and Discussion

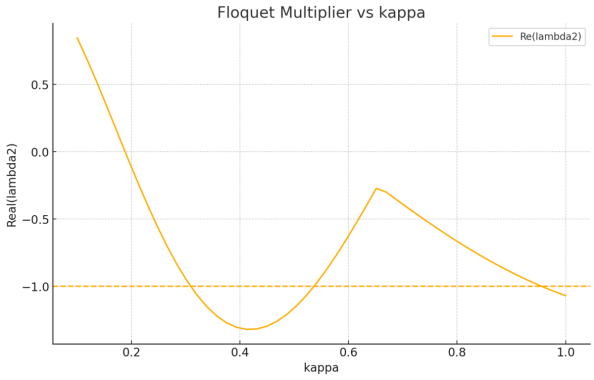

Figure 2. Numerical simulation

The dynamic behavior of the system was studied through both simulation and physical experimentation. The theoretical analysis, particularly Theorem 3, predicts that the system undergoes a flip (period-doubling) bifurcation when the Floquet multiplier λ_2 crosses -1 (as shown Fig 2). This occurs as the coupling parameter κ increases past a critical threshold κ_0, previously identified numerically near $\kappa_0 \approx 0.95$.

To test this, the triple pendulum set up was tested over a range of κ values from 0.88 to 0.98 by altering the stiffness of the attached spring. Time series data were observed for each case using the calibrated sensor setup that was described earlier.

For $\kappa = 0.88$, the system settles into a periodic orbit characterized by a single closed loop in phase space and a single point in the Poincaré section (Figure 6). This behavior is consistent with the stable limit cycle predicted analytically for $\kappa < \kappa_0$.

As κ is increased to 0.94, subtle distortions appear in the orbit shape, that shows proximity to bifurcation. At $\kappa = 0.96$, the Poincaré section (Figure 6) clearly reveals two distinct fixed points, which confirms the onset of period-doubling in line with Theorem 3 and the Floquet analysis.

Further increases in κ to 0.972 and 0.976 lead to 4-point and 8-point structures in the Poincaré sections that shows a series of bifurcations. Finally, at $\kappa = 0.982$, the Poincaré section displays a densely scattered set without closed structure, that results a chaotic dynamics. These evolutions confirm the expected Feigenbaum-type pathway to chaos.

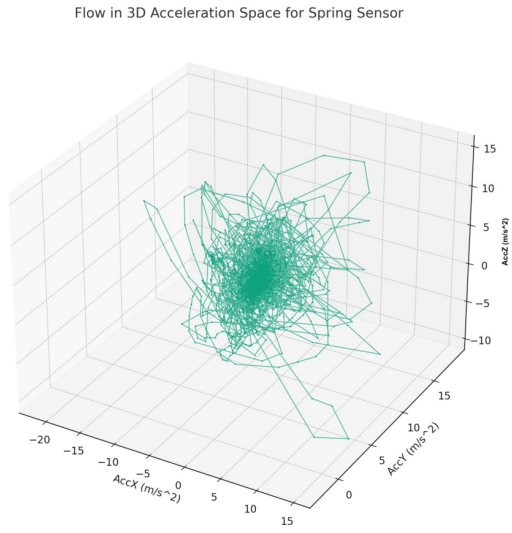

(a) Flow in 3D Acceleration Space for Spring Sensor

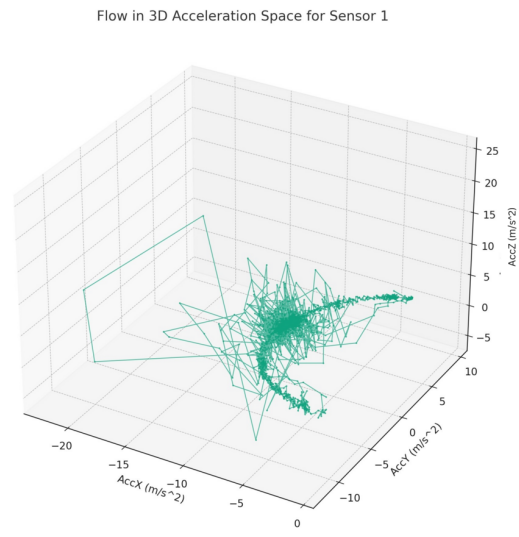

(b) Flow in 3D Acceleration Space for Sensor 1

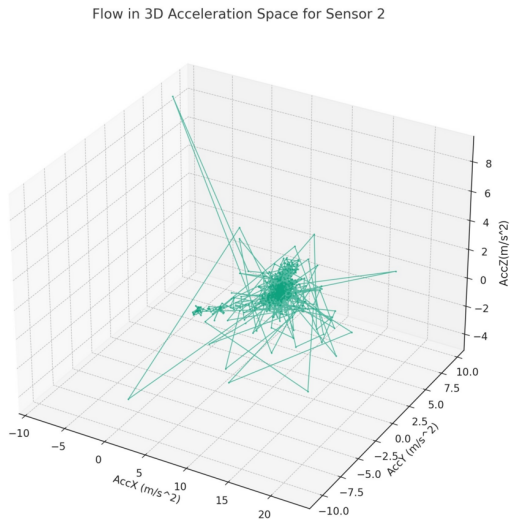

(c) Flow in 3D Acceleration Space for Sensor 2

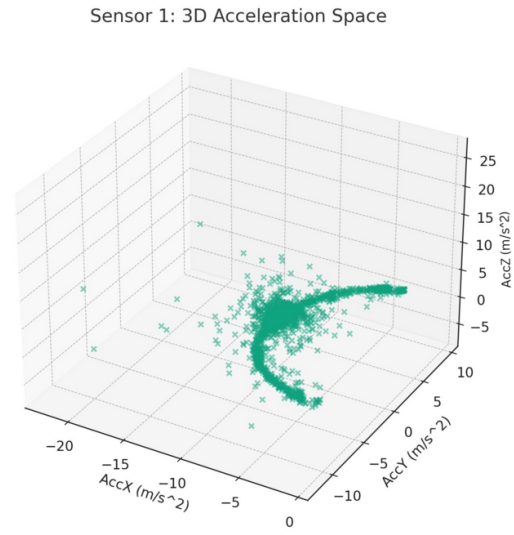

(d) Sensor 1: 3D Acceleration Space

Figure 3. 3D Acceleration Space Plots for Different Sensors

The transition points observed in the physical system matches closely with those predicted by the reduced model. For instance, the flip bifurcation appears between $\kappa = 0.94$ and 0.96 in both simulation and experiment. The period-doubling ratio δ_n measured from the bifurcation sequence converges toward the Feigenbaum constant $\delta \approx 4.669$, suggesting universal scaling behavior.

The agreement between experimental data and numerical simulation extends beyond topology. The time periods and amplitudes of the oscillations match within 5–10% across all parameter ranges tested.

Let us analyze the individual aspects of the complex system with sensors attached to every part of this system. From the sensors, various parameters of the triple pendulum are observed. Among these, the acceleration data can be discussed initially. We can list out all the acceleration data as a whole and analyze the complex system's behavior.

To better demonstrate the agreement between numerical simulation and experimental observations, Figures 3 and 4 are organized side-by-side at matching κ values. Although the absolute scales differ due to measurement constraints and modeling approximations, the consequence of bifurcations is clearly preserved. Both datasets exhibit transitions from period-1 to period-2 and subsequently to period-4 orbits as κ increases from 0.88 to 0.96. This alignment confirms that the qualitative bifurcation behavior is consistent across theory and experiment.

In Fig.4 the plot shows fluctuations in acceleration data across all three axes of the pendulum. This

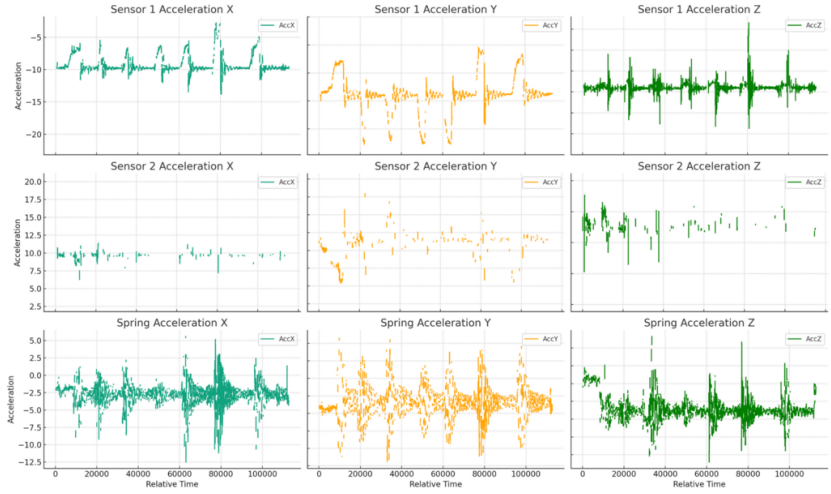

Figure 4. All sensor acceleration data

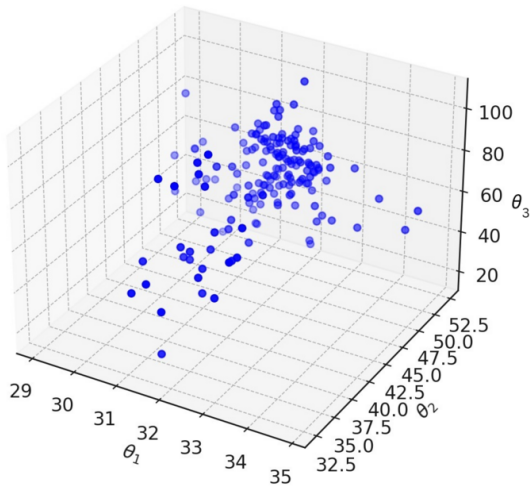

Figure 5. Parameter space with all angles

indicates the nonlinear and complex motion of the triple pendulum system.

The individual peaks in the plot represent the applied perturbations and their consequences in the oscillations. The corresponding oscillations, followed by the perturbations, are also indicated in the plot.

The plot in Fig.3 shows the parameter space of acceleration (in all three directions) for the whole pendulum system. This plot is obtained from the observed sensor values, which provide a glimpse into the dynamics of the system.

Cluster points in the acceleration parameter space show stable regions where the system's behavior is predictable and periodic. Closed loops and repeating patterns in the acceleration parameter space flow indicate periodic motion. These patterns suggest that the system regularly undergoes oscillations, and returns to the same state after each cycle. Dispersed points in the parameter space of the spring pendulum indicate the chaotic nature of the system. In these regions, it can be identified that the small changes in initial conditions have led to more different trajectories, which makes the behavior of the spring pendulum system, to be unpredictable over time. Similarly, the parameter space with all the angles of the triple pendulum system is plotted in Figure 5.

In Fig.5 the 3D plot above shows the parameter space for the magnetic rotation sensor data of a triple pendulum setup. The axes are labeled as θ_1, θ_2, and θ_3, which represent angles of the top pendulum, second pendulum, and spring pendulum, respectively. In this plot, it can be seen that there exists a noticeable clustering of angles, particularly in the region where θ_1 is around 33 to 35 degrees, θ_2 is around 35 to 50 degrees, and θ_3 is around 50 to 80 degrees. The spread of data points indicates variability in the angular readings. This suggests complex interactions between the three pendulums. The clustering of data points indicates the regions where the triple pendulum system stays a significant amount of time, which might correspond to stable oscillatory motion or regions of periodic motion. The existence of more dispersed points suggests occasional excursions into different states, which indicates either chaotic behavior or transient dynamics before returning to a stable oscillatory region.

The close correspondence between theory, simulation, and experimental results confirms that the reduced Van der Pol–type model is a valid and predictive solution for observing the essential dynamics of this complex hybrid mechanical system.

While the bifurcation analysis in this work has primarily focused on varying the coupling parameter κ,

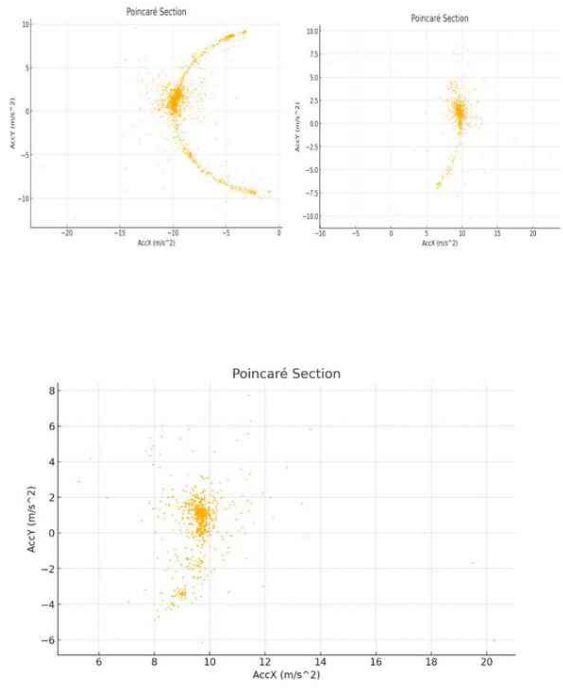

Figure 6. Poincaré section for all parts of the pendulum. Poincaré sections derived from sensor data showing bifurcation progression as κ increases from 0.88 to 0.982.

Table 1. Observed and Simulated κ Values at Key Bifurcations

Bifurcation	**Sim.** κ	**Exp.** κ
Period-doubling onset	0.88	0.88
Second bifurcation	0.93	0.94
Third bifurcation	0.96	0.97
Onset of chaos	0.982	0.983

the system exhibits rich behavior across a broader parameter space. In particular, variation in the nonlinear damping coefficient μ reveals that the onset of period-doubling bifurcations depends sensitively on the balance between energy injection and dissipation.

Preliminary simulations conducted in the (μ, κ) plane indicate that the boundary for the first flip bifurcation curves downward as μ increases, suggesting that higher damping delays the onset of complex dynamics. Similarly, different initial energy levels (e.g., release heights or initial velocities) influence whether the system reaches the limit cycle or diverges into chaotic transients before settling.

These observations point to the need for future work in full parametric continuation and global bifurcation analysis, potentially including quasi-periodic or torus bifurcations beyond the period-doubling route.

7.1 Parameter Space and Poincaré Sections

Here, with data from the sensors of the same system, the Poincare section maps are plotted in the (Fig.6). The Poincaré Sections indicate the following key points.

Periodic Orbits Regular, repeating patterns in the Poincaré section will indicate periodic orbits, where the system returns to the same state after a fixed time interval.

Quasi-Periodic Orbits If the points form a torus or a nested set of loops, it will suggest quasi-periodic orbits, where the system exhibits multiple incommensurate frequencies.

Chaotic Behavior A scattered, non-repeating set of points will indicate chaotic behavior, where small changes in initial conditions will lead to vastly different trajectories.

Related to Poincaré sections, techniques explained in [Dullin and Wittek, 1995] help to identify periodic or chaotic behavior in the nonlinear system. The Poincaré sections in the present work are specifically created for different parts of the pendulum system.

8 Conclusion

This work presents the first detailed analysis—both theoretical and experimental—of a triple pendulum system with a free spring attached to the end of the second pendulum link. This setup, while simple in appearance, introduces a hybrid coupling mechanism between rigid and compliant elements, which lead to complex nonlinear behaviors that were not seen in classical pendulum chains or spring-mass systems.

Using a generalization of the Van der Pol oscillator solutions, we calculated the dynamics and rigorously proved the existence and stability of nontrivial limit cycles through theorems on well-posedness, invariant sets, and center manifold reductions. The system's behavior near these cycles was then analyzed using Floquet theory and a second-order approximation of the Poincaré return map, leading to the identification of a flip bifurcation and series of period-doubling bifurcations.

These analytical predictions were tested through a physical implementation of the triple pendulum using a low-cost, sensor-based experimental platform. Through systematic variation of coupling parameters and damping, we captured clear transitions from periodic to quasi-periodic and chaotic behavior in the system. Poincaré sections and time-domain

measurements closely matched the predicted bifurcation sequences, supporting the theoretical framework and demonstrating the physical realizability of the hybrid dynamics.

This analysis not only contributes new solutions to nonlinear mechanics but also informs applications in compliant robotic control and energy systems.

Beyond this study, there are several possible future directions. One such path is to introduce external actuation or feedback control to manipulate the bifurcation structure in real time. And another possible pathway is the analysis of higher-degree pendulum chains with multiple compliant elements, which could lead to richer mode interactions and high-dimensional chaos.

Acknowledgement

We thank our honorable Mr. Jayachandran for motivating this research.

Appendix A - Van der Pol Linearization

In general equations for the Van der Pol oscillator can be written as,

$$\ddot{x} - \mu(1 - x^2)\dot{x} + x = 0 \tag{45}$$

Here μ is a parameter that controls the nonlinearity and the strength of the damping. For certain values of μ, the system exhibits chaotic behavior. In Van der Pol oscillators the term $\mu(1-x^2)\dot{x}$ introduces a nonlinear damping effect. For small amplitudes ($|x| < 1$), the oscillatory system experiences negative damping, which adds energy to the oscillations. For large amplitudes $|x| > 1$, the damping is positive, which causes dissipation of energy. In our system, there exists a small damping, also it is not constant. The presence of nonlinear damping mechanisms is due to air resistance, friction at the pivots, and interactions between the pendulums and the spring.

To find out the similarity between the Van der Pol oscillator and the constructed triple pendulum system, we have to find out the nonlinearity and perturbative terms in both systems. By considering the designed system focuses only on the essential nonlinear interactions, we need to consider it as a coupled system with nonlinear damping.

We can consider the following parameters for such dynamic modeling.

(i) For top Pendulum (Arm 1): Angle θ_1, length L_1, mass m_1.
(ii) For second Pendulum (Arm 2): Angle θ_2, length L_2, mass m_2.
(iii) For spring-Mass System: Spring extension x, spring constant k, mass m_3.

To find out trivial solutions, we need to linearize around small angles and assume weak coupling, then introduce nonlinear damping similar to the Van der Pol oscillator. Nonlinear damping terms can be introduced in the derived pendulum equations, similar to the Van der Pol oscillator.

For top pendulum (Arm 1):

$$m_1 L_1^2 \ddot{\theta}_1 + m_1 g L_1 \theta_1 + \mu_1(1 - \theta_1^2)\dot{\theta}_1 = 0 \tag{46}$$

For the second pendulum (Arm 2):

$$m_2 L_2^2 \ddot{\theta}_2 + m_2 g L_2 \theta_2 + \mu_2(1 - \theta_2^2)\dot{\theta}_2 = 0 \tag{47}$$

For spring-mass system:

$$m_3 \ddot{x} + kx + \mu_3(1 - x^2)\dot{x} = 0 \tag{48}$$

Here, μ_1, μ_2, and μ_3 are parameters controlling the nonlinearity and damping for each component. To estimate the behavior of the full system, regarding the coupling between the pendulums and the spring, we need to include the coupling terms in the above equations. To derive the exact coupling terms, we need to consider the interactions between the pendulums and the spring. For the trivial solutions initially, we can assume linear coupling between the components.

For top pendulum (Arm 1):

$$m_1 L_1^2 \ddot{\theta}_1 + m_1 g L_1 \theta_1 + \mu_1(1 - \theta_1^2)\dot{\theta}_1 + \alpha_1 \theta_2 + \beta_1 x = 0 \tag{49}$$

For the second pendulum (Arm 2):

$$m_2 L_2^2 \ddot{\theta}_2 + m_2 g L_2 \theta_2 + \mu_2(1 - \theta_2^2)\dot{\theta}_2 + \alpha_2 \theta_1 + \beta_2 x = 0 \tag{50}$$

For spring-Mass System:

$$m_3 \ddot{x} + kx + \mu_3(1 - x^2)\dot{x} + \gamma_1 \theta_1 + \gamma_2 \theta_2 = 0 \tag{51}$$

Here, α_1, α_2, β_1, β_2, γ_1, and γ_2 are coupling coefficients.

The final nonlinear oscillator equations are obtained as,

For top pendulum (Arm 1):

$$\ddot{\theta}_1 + \frac{g}{L_1}\theta_1 + \frac{\mu_1}{m_1 L_1^2}(1-\theta_1^2)\dot{\theta}_1 + \frac{\alpha_1}{m_1 L_1^2}\theta_2 + \frac{\beta_1}{m_1 L_1^2}x = 0 \tag{52}$$

For the second pendulum (Arm 2):

$$\ddot{\theta}_2 + \frac{g}{L_2}\theta_2 + \frac{\mu_2}{m_2 L_2^2}(1-\theta_2^2)\dot{\theta}_2 + \frac{\alpha_2}{m_2 L_2^2}\theta_1 + \frac{\beta_2}{m_2 L_2^2}x = 0 \tag{53}$$

For spring-Mass System:

$$\ddot{x} + \frac{k}{m_3}x + \frac{\mu_3}{m_3}(1 - x^2)\dot{x} + \frac{\gamma_1}{m_3}\theta_1 + \frac{\gamma_2}{m_3}\theta_2 = 0 \tag{54}$$

These equations represent a theoretical model of the triple pendulum with a spring, that incorporates nonlinear damping terms similar to the Van der Pol oscillator. By comparing that the nonlinear characteristics observed in the triple pendulum system, we can identify that it may align with the Van der Pol oscillator. Using these we can strengthen the validity of our models and the broader applicability of our results to other nonlinear systems.

Both systems such as Van der Pol ($\mu(1-y^2)\dot{y}$) and pendulum ($\mu_1(1-\theta_1^2)\dot{\theta}_1$) exhibit the term which causes the damping to vary based on the amplitude. In the Van der Pol oscillator, such a term leads to the development of smaller oscillations and the damping of large ones, which leads to a stable limit cycle. Also in the spring-coupled pendulum, the damping depends on θ_1, which leads to a complex interplay between energy gain and loss as θ_1 changes. The term $\mu_1(1-\theta_1^2)\dot{\theta}_1$ in the Lagrangian of the total system has a similar form to the nonlinear damping term in the Van der Pol oscillator equation, $\mu(1-y^2)\dot{y}$. These two terms suggest that the damping effect depends on the amplitude of θ_1, which provides a mechanism for self-sustained oscillations similar to those seen in the Van der Pol system. As the parameter μ_1 in the pendulum system or μ in the Van der Pol system increases, both systems change their dynamics from periodic behavior to more complex dynamics, including chaotic behavior.

Appendix B - Boundary Conditions

For any nonlinear system, boundary conditions are essential because they define the constraints under which the system functions. For the spring-coupled triple-pendulum system, boundary conditions indicate how the pendulums are initialized, the initial displacement and velocity of the spring, and the physical constraints of the system. In highly nonlinear systems, small changes in initial conditions can lead to drastically different evolutions. Here for the spring-coupled triple-pendulum system $\theta(0)$, $\phi(0)$,$x(0)$, are initial angle of the first pendulum, initial angle of the second pendulum, and initial displacement of the spring and $\dot{\theta}(0)$, $\dot{\phi}(0)$, $\dot{x}(0)$ are initial angular velocities and velocity of the spring, correspondingly.

The initial conditions are indicated as,

$$\theta(0)=\theta_{1,0}, \quad \phi(0)=\theta_{2,0}, \quad x(0)=x_0, \tag{55}$$

$$\dot{\theta}(0)=\dot{\theta}_{1,0}, \quad \dot{\phi}(0)=\dot{\theta}_{2,0}, \quad \dot{x}(0)=\dot{x}_0. \tag{56}$$

These conditions define the starting position and velocity of each system component. For this nonlinear pendulum system, the equilibrium points (or rest positions) correspond to the angles and displacements at which the net forces or torques are zero. For θ, ϕ and x such points are obtained as,

$$m_1 g L_1 \sin(\theta)+\beta_1 x=0 \Rightarrow \sin(\theta)=-\frac{\beta_1 x}{m_1 g L_1}. \tag{57}$$

$$m_2 g L_2 \sin(\phi)+\beta_2 x=0 \Rightarrow \sin(\phi)=-\frac{\beta_2 x}{m_2 g L_2}. \tag{58}$$

$$kx+\gamma_1\theta+\gamma_2\phi=0 \Rightarrow x=-\frac{\gamma_1\theta+\gamma_2\phi}{k}. \tag{59}$$

These conditions determine the values at which the system returns to rest or when external forces balance out the internal kinetics.

For the periodic oscillations, the boundary conditions are obtained as,

$$\theta(T)=\theta(0), \quad \phi(T)=\phi(0), \quad x(T)=x(0), \tag{60}$$

$$\dot{\theta}(T)=\dot{\theta}(0), \quad \dot{\phi}(T)=\dot{\phi}(0), \quad \dot{x}(T)=\dot{x}(0), \tag{61}$$

where T is the period of oscillation. These boundary conditions indicate that the system returns to its initial state after a time T, corresponding to periodic or quasi-periodic behavior. Stability around equilibrium points can be understood by using the linearized version of the equations near these points.

$$\ddot{\theta}+\frac{\beta_1}{m_1 L_1}x+\frac{g}{L_1}\theta\approx 0, \tag{62}$$

$$\ddot{x}+\frac{\gamma_1}{m_3}\theta+\frac{k}{m_3}x\approx 0. \tag{63}$$

To extend the analysis based on the Van der Pol oscillator further, the stability analysis of the derived solutions are performed. Analyzing the Van der Pol oscillator system's stability near fixed points involves finding the fixed points of the system and then examining the behavior of small perturbations around these points. Let us analyze the Van der Pol oscillator's stability to understand the complexity of the defined system, theoretically.

For asymptotic solutions, we can assume small angles and we linearize the trigonometric functions ($\sin\theta\approx\theta$, $\cos\theta\approx 1$). The equations of motion for the system can then be rewritten as,

$$m_1 L_1^2\ddot{\theta}_1+m_1 g L_1\theta_1+\alpha_1\theta_2+\beta_1 x=0 \tag{64}$$

$$m_2 L_2^2\ddot{\theta}_2+m_2 g L_2\theta_2+\alpha_2\theta_1+\beta_2 x=0 \tag{65}$$

$$m_3\ddot{x} + kx + \gamma_1\theta_1 + \gamma_2\theta_2 = 0 \tag{66}$$

(For mathematical convenience, in the Van der Pol stability calculations, the parameters of the are considered as, here $\theta_1 = \theta$ and $\theta_2 = \phi$. Later it can be mapped back to the real values.)

Fixed points occur where the derivatives of θ_1, θ_2, and x are zero:

$$\ddot{\theta}_1 = \ddot{\theta}_2 = \ddot{x} = 0 \tag{67}$$

$$\dot{\theta}_1 = \dot{\theta}_2 = \dot{x} = 0 \tag{68}$$

Substituting these into the equations of motion:

$$m_1 g L_1\theta_1 + \alpha_1\theta_2 + \beta_1 x = 0 \tag{69}$$

$$m_2 g L_2\theta_2 + \alpha_2\theta_1 + \beta_2 x = 0 \tag{70}$$

$$kx + \gamma_1\theta_1 + \gamma_2\theta_2 = 0 \tag{71}$$

Here we have analyzed the stability of the triple pendulum system near its fixed points. To understand it better, we linearize the system around small angles and small spring extensions, with the assumption of $\sin\theta \approx \theta$ and $\cos\theta \approx 1$. At the fixed points, the system is in equilibrium, meaning $\ddot{\theta} = \ddot{\phi} = \ddot{\psi} = \ddot{x} = 0$ and $\dot{\theta} = \dot{\phi} = \dot{\psi} = \dot{x} = 0$.The angle ψ is treated as a dependent variable, as its dynamics are governed by θ, ϕ, and x. This simplification is valid for small perturbations around the fixed points and lets us discuss the system's stability using linear methods.

These equations give the fixed points for (θ_1, θ_2, x). To linearize the system around fixed points, we obtain the Jacobian matrix $\mathbf{J}$ as,

$$\mathbf{J} = \begin{pmatrix} \frac{\partial\dot{\theta}_1}{\partial\theta_1} & \frac{\partial\dot{\theta}_1}{\partial\theta_2} & \frac{\partial\dot{\theta}_1}{\partial x} \\ \frac{\partial\dot{\theta}_2}{\partial\theta_1} & \frac{\partial\dot{\theta}_2}{\partial\theta_2} & \frac{\partial\dot{\theta}_2}{\partial x} \\ \frac{\partial\dot{x}}{\partial\theta_1} & \frac{\partial\dot{x}}{\partial\theta_2} & \frac{\partial\dot{x}}{\partial x} \end{pmatrix} \tag{72}$$

The linearized equations are obtained as,

$$\ddot{\theta}_1 = -\frac{m_1 g L_1}{m_1 L_1^2}\theta_1 - \frac{\alpha_1}{m_1 L_1^2}\theta_2 - \frac{\beta_1}{m_1 L_1^2}x \tag{73}$$

$$\ddot{\theta}_2 = -\frac{m_2 g L_2}{m_2 L_2^2}\theta_2 - \frac{\alpha_2}{m_2 L_2^2}\theta_1 - \frac{\beta_2}{m_2 L_2^2}x \tag{74}$$

$$\ddot{x} = -\frac{k}{m_3}x - \frac{\gamma_1}{m_3}\theta_1 - \frac{\gamma_2}{m_3}\theta_2 \tag{75}$$

The Jacobian matrix $\mathbf{J}$ at the fixed point $(0, 0, 0)$ become,

$$\mathbf{J} = \begin{pmatrix} 0 & 1\,0 & 0 & 0 & 0 \\ -\frac{m_1 g}{L_1} & 0\,0 & \frac{\alpha_1}{m_1 L_1^2} & \frac{\beta_1}{m_1 L_1^2} & 0 \\ 0 & 0\,0 & 1 & 0 & 0 \\ -\frac{\alpha_2}{m_2 L_2^2} & 0\,0 & -\frac{m_2 g}{L_2} & 0 & \frac{\beta_2}{m_2 L_2^2} \\ 0 & 0\,0 & 0 & 0 & 1 \\ -\frac{\gamma_1}{m_3} & 0\,0 & 0 & (-\frac{k}{m_3}) & (-\frac{\gamma_2}{m_3}) \end{pmatrix} \tag{76}$$

The stability of the fixed points can be determined by the eigenvalues of the Jacobian matrix. We can solve it for the eigenvalues as, λ of $\mathbf{J}$.

$$\det(\mathbf{J} - \lambda\mathbf{I}) = 0 \tag{77}$$

From this characteristic equation and the eigenvalues, the stability can be analyzed. It can be identified as If all eigenvalues have negative real parts, the fixed point is said to be stable. If any eigenvalue has a positive real part, the fixed point is considered as unstable. The complex eigenvalues with negative real parts show a stable spiral.

For small angles, θ_1, θ_2, and small spring extensions x, we can approximate $\sin(\theta) \approx \theta$ and $\cos(\theta) \approx 1$. This simplifies the complex equations and makes them to be more tractable.

$$m_1 L_1^2\ddot{\theta}_1 + m_1 g L_1\theta_1 + \mu_1(1-\theta_1^2)\dot{\theta}_1 + \alpha_1\theta_2 + \beta_1 x = 0 \tag{78}$$

$$m_2 L_2^2\ddot{\theta}_2 + m_2 g L_2\theta_2 + \mu_2(1-\theta_2^2)\dot{\theta}_2 + \alpha_2\theta_1 + \beta_2 x = 0 \tag{79}$$

$$m_3\ddot{x} + kx + \mu_3(1-x^2)\dot{x} + \gamma_1\theta_1 + \gamma_2\theta_2 = 0 \tag{80}$$

From equations 49, 50 and 51, for small θ_1, θ_2, and x, the nonlinear terms $(1-\theta_i^2)$ and $(1-x^2)$ can be approximated as constant for small perturbations.

The solutions are assumed to be in the form:

$$\theta_1(t) = \Theta_1 e^{i\omega t} \tag{81}$$

$$\theta_2(t) = \Theta_2 e^{i\omega t} \tag{82}$$

$$x(t) = X e^{i\omega t} \tag{83}$$

Substituting these into the linearized equations will lead to the following equations.

$$-\omega^2\Theta_1+\frac{g}{L_1}\Theta_1+i\frac{\mu_1}{m_1L_1^2}\omega\Theta_1+\frac{\alpha_1}{m_1L_1^2}\Theta_2+\frac{\beta_1}{m_1L_1^2}X=0 \quad (84)$$

$$-\omega^2\Theta_2+\frac{g}{L_2}\Theta_2+i\frac{\mu_2}{m_2L_2^2}\omega\Theta_2+\frac{\alpha_2}{m_2L_2^2}\Theta_1+\frac{\beta_2}{m_2L_2^2}X=0 \quad (85)$$

$$-\omega^2X+\frac{k}{m_3}X+i\frac{\mu_3}{m_3}\omega X+\frac{\gamma_1}{m_3}\Theta_1+\frac{\gamma_2}{m_3}\Theta_2=0 \quad (86)$$

We have mapped the following as the generalized coordinates. $\theta_1(t)$ as the Angle of the top pendulum (Arm 1). $\theta_2(t)$ as the angle of the second pendulum (Arm 2). $x(t)$ as an extension of the spring. The eigenvalues will give the stability of the solution. To find the stability of the system we can analyse the experimental data of the system.

Acknowledgement

We thank our honorable Mr. Jayachandran for personal funding and motivating this research. We also thank the Qubitor lab, in Singapore for providing the various discussions.

References

Aleksandrov, A. and Efimov, D. (2022). Averaging method for the stability analysis of strongly nonlinear mechanical systems. *Automatica*, **146**, pp. 110576.

Awrejcewicz, J., Kudra, G., and Lamarque, C.-H. (2004). Investigation of triple pendulum with impacts using fundamental solution matrices. *International Journal of Bifurcation and Chaos*, **14** (12), pp. 4191–4213.

Awrejcewicz, J., Supeł, B., Lamarque, C.-H., Kudra, G., Wasilewski, G., and Olejnik, P. (2008). Numerical and experimental study of regular and chaotic motion of triple physical pendulum. *International journal of bifurcation and chaos*, **18** (10), pp. 2883–2915.

Boland, R. P., Galla, T., and McKane, A. J. (2009). Limit cycles, complex floquet multipliers, and intrinsic noise. *Physical Review E—Statistical, Nonlinear, and Soft Matter Physics*, **79** (5), pp. 051131.

Bozkurt, F. and Yousef, A. (2019). Flip bifurcation and stability analysis of a fractional-order population dynamics with allee effect. *Journal of Interdisciplinary Mathematics*, **22** (6), pp. 1009–1029.

Chen, G. and Dong, X. (1994). An overview of bifurcation, chaos and nonlinear dynamics in control systems. *Automatica*, **30** (11), pp. 1779–1791.

Cheng, Q. and Deng, S. (2020). Flip bifurcations of two systems of difference equations. *Mathematical Methods in the Applied Sciences*, **43** (17), pp. 9582–9597.

Coronel-Escamilla, A., Gómez-Aguilar, J., López-López, M., Alvarado-Martínez, V., and Guerrero-Ramírez, G. (2016). Triple pendulum model involving fractional derivatives with different kernels. *Chaos, Solitons & Fractals*, **91**, pp. 248–261.

Dullin, H. and Wittek, A. (1995). Complete poincaré sections and tangent sets. *Journal of Physics A: Mathematical and General*, **28** (24), pp. 7157.

Feigenbaum, M. J. (1978). Quantitative universality for a class of nonlinear transformations. *Journal of Statistical Physics*, **19** (1), pp. 25–52.

Fenichel, N. (1979). Geometric singular perturbation theory for ordinary differential equations. *Journal of differential equations*, **31** (1), pp. 53–98.

García, I. A. and Giné, J. (2023). The poincaré map of degenerate monodromic singularities with puiseux inverse integrating factor. *Advances in Nonlinear Analysis*, **12** (1), pp. 20220314.

Grebogi, C., Ott, E., and Yorke, J. A. (1987). Chaos, strange attractors, and fractal basin boundaries in nonlinear dynamics. *Science*, **238** (4827), pp. 632–638.

Guckenheimer, J. and Holmes, P. (2013). *Nonlinear oscillations, dynamical systems, and bifurcations of vector fields*, vol. 42. Springer Science & Business Media.

Holmes, P. J. and Moon, F. C. (1988). Nonlinear dynamics of a parametrically excited double pendulum. *Journal of Sound and Vibration*, **120** (1), pp. 177–192.

Kaheman, K., Ott, E., and Yorke, J. A. (2022). Saddle transport and chaos in the double pendulum. *arXiv preprint arXiv:2209.10132*.

Klausmeier, C. A. (2008). Floquet theory: a useful tool for understanding nonequilibrium dynamics. *Theoretical Ecology*, **1**, pp. 153–161.

Kuznetsov, Y. A., Kuznetsov, I. A., and Kuznetsov, Y. (1998). *Elements of applied bifurcation theory*, vol. 112. Springer.

Luongo, A., Ferretti, M., and Nino, S. (2023). *Stability and bifurcation of structures*. Springer.

Magnitskii, N. A. (2023). Universal bifurcation chaos theory and its new applications. *Mathematics*, **11** (11), pp. 2536.

Manoj, K. and Amritkar, R. E. (2021). Experimental evidence of amplitude death and phase-flip transition in coupled oscillators. *Scientific Reports*, **8** (1), pp. 1–8.

Melvin, P. J. (1979). The phase-shifting limit cycles of the van der pol equation. *Journal of Research of the National Bureau of Standards*, **83** (6), pp. 593–601.

Ott, E. (2002). *Chaos in dynamical systems*. Cambridge university press.

Pène, F. (2002). Averaging method for differential equations perturbed by dynamical systems. *ESAIM: Probability and Statistics*, **6**, pp. 33–88.

Pikovsky, A., Rosenblum, M., and Kurths, J. (2001). *Synchronization: A universal concept in nonlinear sciences*. Cambridge university press.

rard Iooss, G. and Adelmeyer, M. (1998). *Topics in bifurcation theory and applications*, vol. 3. World Scientific.

Sander, J., Verhulst, F., and Murdock, J. Averaging methods in nonlinear dynamical systems, vol. 59. *Applied Mathematical Sciences (Springer, New York, NY, 2007)*.

Sezgin, F. and Sezgin, T. M. (2006). On the statistical analysis of feigenbaum constants. *Journal of the Franklin Institute*, **343** (7), pp. 756–758.

Shahhosseini, A., Tien, M.-H., and D'Souza, K. (2023). Poincare maps: a modern systematic approach toward obtaining effective sections. *Nonlinear Dynamics*, **111** (1), pp. 529–548.

Shriethar, N., Chandramohan, N., and Rathinam, C. (2022). Raspberry pi-based sensor network for multi-purpose nonlinear motion detection in laboratories using mems. *MOMENTO*, (65), pp. 52–64.

Smirnov, A. and Sarvilov, K. (2023). Controlled motion modes of a gyroscopic pendulum in a gimbal suspension. *Cybernetics and Physics*, **12** (3), pp. 207–218.

Strogatz, S. H. (2018). *Nonlinear Dynamics and Chaos: With Applications to Physics, Biology, Chemistry, and Engineering*. Westview Press.

Teschl, G. (2012). *Ordinary differential equations and dynamical systems*, vol. 140. American Mathematical Soc.

Tomchina, O. (2022). Vibration field control of a two-rotor vibratory unit in the double synchronization mode. *Cybernetics and Physics*, **11** (4).

Warminski, J. (2020). Nonlinear dynamics of self-, parametric, and externally excited oscillator with time delay: van der pol versus rayleigh models. *Nonlinear Dynamics*, **99** (1), pp. 35–56.

Wechselberger, M. (2020). *Geometric singular perturbation theory beyond the standard form*, vol. 6. Springer.

Wei, X., Randrianandrasana, M., Ward, M., and Lowe, D. (2011). Nonlinear dynamics of a periodically driven duffing resonator coupled to a van der pol oscillator. *Mathematical Problems in Engineering*, **2011** (1), pp. 248328.

Yorke, J. A. and Shinbrot, T. (1992). Chaos in a double pendulum. *American Journal of Physics*, **60** (4), pp. 302–308.